# Scale Resolving Simulations of Contra Rotating Open Rotor Noise Prediction

Ercan Dumlupinar*, Jeffrey A. Housman†, Jared C. Duensing‡
*NASA Ames Research Center, Moffett Field, CA 94035*

**The development of breakthrough open-rotor propulsion systems that meet performance, fuel efficiency, and noise requirements for commercial viability relies heavily on the availability of reliable and computationally efficient aerodynamic performance and noise prediction tools. This investigation showcases the proficiency of the structured curvilinear overset grid Computational Fluid Dynamics solver implemented in the Launch, Ascent, and Vehicle Aerodynamics framework for predicting the aerodynamic and aeroacoustic characteristics of a Contra-Rotating Open Rotor propulsion system. Additionally, the study includes comprehensive sensitivity analyses employing a Hybrid Reynolds-Averaged Navier-Stokes/Large Eddy Simulation - based scale-resolving turbulence closure treatment. The computed results are validated through comparison with existing experimental measurements.**

## I. Introduction

The growing concerns about the environment and the rising costs of energy have brought open-rotor propulsion systems into the spotlight as a potential solution for future commercial transport aircraft. These systems present substantial efficiency improvements compared to modern turbofan engines, owing to their ultra-high bypass ratios and reduced losses. Enhancing the efficiency of propulsion systems is crucial for reducing fuel consumption and lowering $CO_2$ emissions, aligning with the aviation industry's commitment to greater environmental sustainability. Consequently, well-crafted next-generation open-rotor concept propulsors could play a pivotal role in meeting market-driven objectives for fuel burn and noise reduction, serving as an integral component in the development of a new single-aisle aircraft in the 2030s. The aim of this publication is to showcase the readiness of analysis tools for investigating the aerodynamic and aeroacoustic behavior of experimentally well-documented Contra-Rotating Open Rotor (CROR) propulsion systems. The primary focus is on conducting a sensitivity analysis of the system under nominal takeoff conditions and demonstrating the impact of acoustic plate effects on noise prediction during cruise speed tests. This analysis utilizes a high-fidelity Computational Fluid Dynamics (CFD) solver integrated within the Launch, Ascent, and Vehicle Aerodynamics (LAVA) framework[1, 2].

Several researchers [3–7] have reported noise predictions from a CROR propulsion system using a model scale version of the General Electric (GE) F31/A31 blade set. Envia [3] utilized a commercially available software package along with a NASA-developed acoustic propagation code to simulate a single blade passage for each rotor row, studying the acoustic behavior of the CROR system at cruise flight conditions. Housman and Kiris [4] used the structured overlapping curvilinear LAVA solver to model the full annulus of the forward and aft rotor blade rows along with the hub in a three-dimensional time-accurate moving mesh simulation of the CROR system at the cruise condition, similar to Envia [3]. Housman and Kiris [4] employed finite-difference discretizations and a Delayed Detached Eddy Simulation (DDES) approach for turbulence closure to increase the modeling fidelity. However, pre-computing the dynamic overset grid connectivity required excessive memory, file I/O, and mode time-step, making sensitivity studies challenging. Brehm et al. [5, 6] performed an aeroacoustic analysis using the Cartesian grid immersed boundary methodology, also available in the LAVA framework. Nark et al. [7] analyzed the low-speed (take-off) configuration using two additional NASA-developed CFD codes, OVERFLOW and FUN3D. Recently, Dumlupinar et al. [8] conducted a study demonstrating a newly implemented sliding mesh approach for predicting aerodynamic forces and tonal noise generated by a CROR. The study focused on both nominal takeoff and cruise flight conditions using a scaled model. To perform the simulations, the researchers utilized the curvilinear structured overset finite-difference solver within the LAVA framework, employing both Unsteady Reynolds-Averaged Navier-Stokes (URANS) and Hybrid Reynolds-Averaged Navier-Stokes/Large Eddy Simulation (HRLES) turbulence closures. This approach allowed for a comprehensive

*Computational Aerosciences Branch, AIAA Senior Member, ercan.dumlupinar@nasa.gov
†Computational Aerosciences Branch, AIAA Senior Member, jeffrey.a.housman@nasa.gov
‡Computational Aerosciences Branch, AIAA Member, jared.c.duensing@nasa.gov

analysis of the flow characteristics and noise generation associated with the CROR system. In the present work, the structured curvilinear overset finite-difference solver in LAVA is employed to determine the most effective approach for conducting HRLES-based scale-resolving simulations of a CROR propulsion system. The first objective is to investigate various sensitivity studies for low-speed test conditions, with the goal of optimizing the simulation settings to achieve accurate and reliable results. The impact of the acoustic plate on tonal and broadband noise is then investigated in the cruise configuration, where the acoustic plate serves as the holder for the Kulite pressure sensors in the experimental study. The computed results are rigorously validated against existing experimental measurements obtained from nominal take-off and cruise flight conditions.

This paper is structured into several sections. In Section II, the geometry of the open-rotor configuration is specified, and the experimental measurement conditions are described. Section III provides a thorough description of the computational methodology employed and a concise overview of the turbulence closure treatment utilized in the simulations. Section IV presents the details of the structured overlapping grid system implemented in the analysis. Additionally, the permeable acoustic surface, which plays a significant role in the study, is discussed in this section. Section V is dedicated to presenting the computed results obtained from the simulations. These results are compared to the experimental data, providing a comprehensive evaluation of the accuracy and reliability of the computational approach. Finally, in Section VI, concluding remarks are provided, summarizing the key findings and implications of the study.

## II. Geometry and Test Conditions

The CROR configuration utilized in this study was derived from the General Electric (GE) F31/A31 model, featuring twelve blades in the front row and ten blades in the aft row. Throughout the experimental measurement campaign, NASA wind tunnels were employed to gather extensive aerodynamic and acoustic data for a model-scale version of this configuration, spanning various flight conditions. The model-scale blade rows were approximately 0.2 meters apart, with blade tip diameters of 0.66 and 0.63 meters for the forward and aft rows, respectively. Employing a slightly shorter blade in the aft row served to diminish the risk of impingement of the forward blade tip vortices on the aft blade row, thereby preventing Blade Vortex Interaction (BVI) noise.

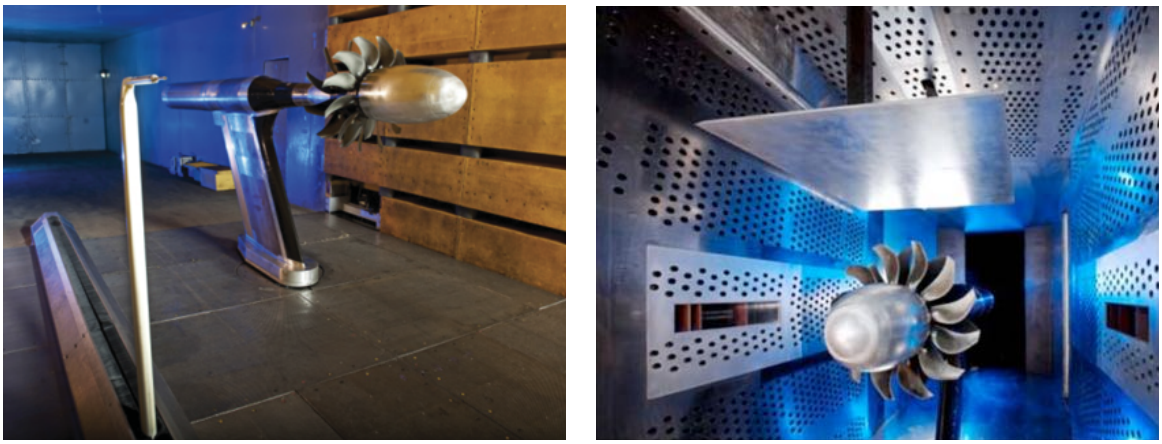
In this study, two flight condition cases, identified as nominal takeoff and cruise, were examined and compared with corresponding experimental measurements. The blade planform geometry and spacing remained consistent for both flight conditions, but variations existed in blade pitch angles and inflow Mach numbers. The nominal takeoff – low-speed – experiment involved investigating the noise and aerodynamic performance of the model-scale CROR within NASA's 9 by 15 ft acoustic wind tunnel, as depicted in Figure 1 (a). In the low-speed case, forward and aft blade pitch angles were set at 40.1 and 40.8 degrees, respectively, with a constant rotation at 6303 RPM and an inflow Mach number of 0.2.

Cruise configuration – high-speed – aerodynamics and acoustic data were collected for a model-scale geometry in NASA's 8 by 6 ft Supersonic Wind Tunnel, focusing on documenting the cruise performance of the CROR, as shown in Figure 1 (b). During this flight condition, the tunnel's inflow Mach number was set to 0.78, with forward and aft blade pitch angles at 64.4 and 61.8 degrees, respectively. Both blade rows rotated at a constant 6848 RPM. Acoustic measurements in the 8 by 6 ft tunnel were obtained from 17 flush-mounted Kulite sensors on a plate positioned over the model at five different vertical distances [3, 9].

## III. Computational Methodology

The computational studies in this work utilized the structured overset CFD solver within the LAVA framework. The LAVA structured overset solver was constructed based on a finite-difference formulation, implementing the general non-orthogonal curvilinear transformed system of compressible Navier-Stokes equations in strong conservation law form. In continuation of previous work [8], the HRLES approach was employed as a turbulence closure treatment to predict tonal noise generated by the contra-rotating open rotor (CROR) propulsion system. A brief overview of the related numerical discretization and turbulence closure treatment is provided in this section.

The low-speed flight configuration simulation was conducted using a third-order accurate modified Roe scheme to discretize the convective fluxes; while a modified third-order upwind scheme for high-speed flow (HSUW) [10] was utilized for the high-speed flight condition along with a local shock sensor based WENO limiter, denoted *wenoshkfr*. The *wenoshkfr* limiter employed the minimum pressure gradient-based shock sensor and the Ducros sensor to minimize the artificial dissipation in the turbulence-resolving region. When the sensors detected a shock, the HSUW scheme switched from its standard modified Roe numerical flux to a more robust HLL numerical flux. The discretization of the



(a) (b)

**Fig. 1 (a) CROR installed in 9 by 15 ft Low Speed Acoustic Wind Tunnel[9], (b) CROR installed in 8 by 6 ft Supersonic Wind Tunnel[9].**

viscous fluxes was based on the second-order accurate midpoint and node central differencing.

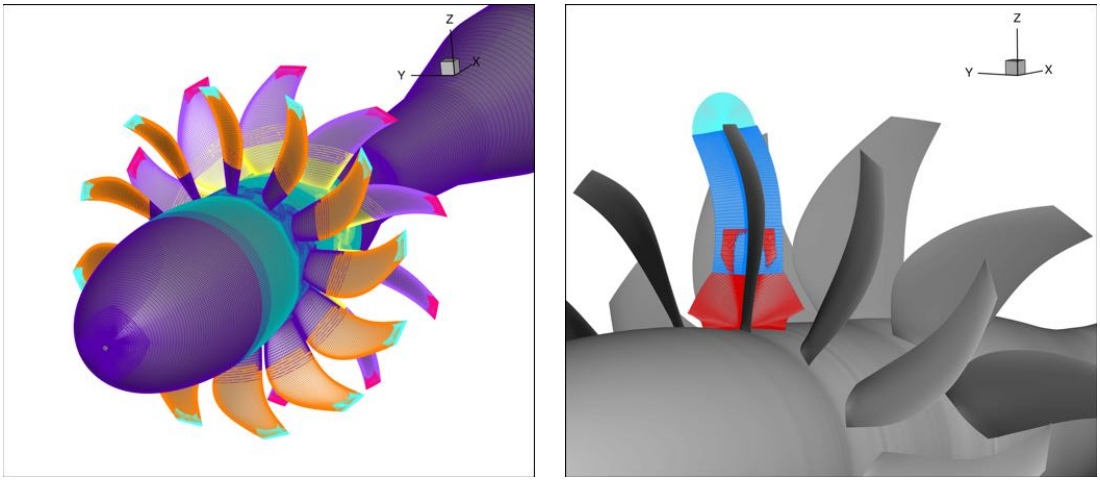
The HRLES approach employed in this work was the Zonal Detached Eddy Simulation (ZDES) 2020 Enhanced Protection method[11], featuring an improved shielding function compared to its predecessor. The same SA-neg turbulence model with RC and QCR2000 corrections was used as the base RANS closure model. The turbulence model equations effectively reduced to a Smagorinsky-like sub-grid scale model in regions designated as LES based on the shielding function. HRLES simulations in the LAVA computational framework were extensively validated for various aerodynamic applications[4, 8, 12, 13]. For temporal discretization, an implicit second-order backward differencing (BDF2) was used in physical time, and the discretized equations were marched in pseudo-time to a converged solution for each physical time step. The nonlinear system of equations was linearized at each pseudo-time-step, and an ILU(1) preconditioned generalized minimal residual method (GMRES) algorithm was used to solve the resulting linear system.

The Ffowcs Williams-Hawkings (FW-H) model[14], a linear acoustic propagation model, was used to propagate the acoustics generated from the near-field CFD simulations. Permeable and non-permeable frequency domain FW-H formulations were implemented in LAVA, utilizing an unstructured surface triangulation embedded within the structured overlapping grid system for evaluation.

## IV. Structured Overset Grid System and Permeable Surfaces

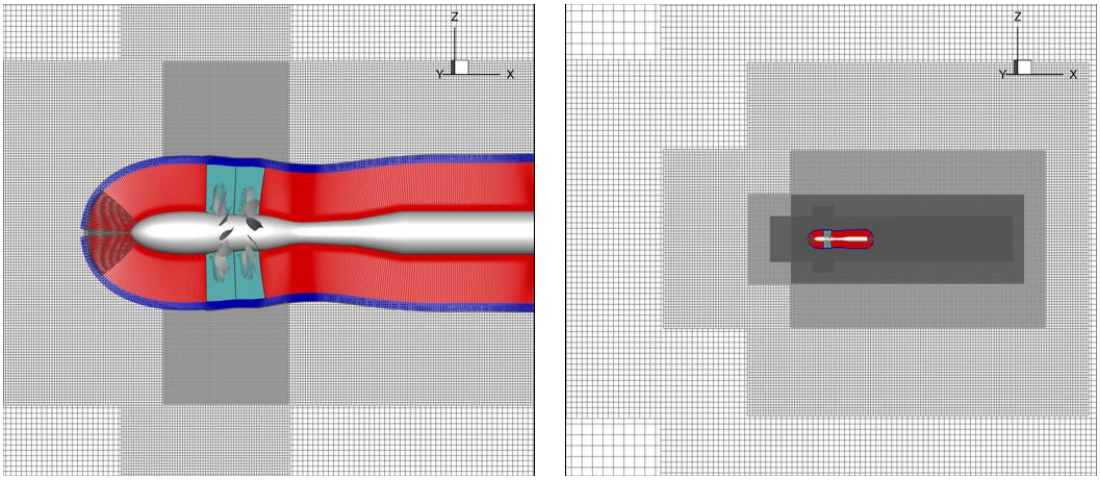
In the present study, meshes were constructed using a structured curvilinear overlapping grid methodology. The advantage of this approach for viscous analysis lay in the ability to generate highly anisotropic grids capable of capturing boundary layers, wakes from the blades, and tip vortices. Allowing the structured grids to overlap each other simplified generating the grids compared to structured purely multi-block patched grids. The structured curvilinear approach also allows for high-quality (less-skewed) meshes and a modular approach to adding both geometric components and anisotropic meshes for resolving essential flow features. Furthermore, combining the overset grid methodology with sliding multi-block mesh interfaces had the inherent ability to capture relative motion effects while enabling the usage of highly efficient numerical algorithms with high-order, low-dissipation convective flux discretization, necessary to capture flow/acoustic coupling.

A script for the structured overset grid system of the GE F31/A31 CROR model was developed using the Chimera Grid Tools (CGT) software package[15, 16]. This script can generate a fully automated mesh for various flight conditions. The grid system contained at least double fringe layers to accommodate the low dissipative finite-difference discretizations up to fourth-order accuracy available in the solver. Figure 2 shows images of the low-speed flight configuration surface and volume grids. The octree-based overlapping off-body Cartesian grid is generated automatically using a built-in module in the LAVA framework. The primary benefit of having octree-based Cartesian off-body mesh is the ability to set different mesh refinements in the vicinity of the specific components of the configuration. Using this method reduces the number of grid points used in an off-body mesh while keeping grid quality high. Global views




(a) (b)

**Fig. 2 Several views of overset grid system for low-speed configuration (a) isometric view of the surface, and (b) slices of the forward blade volume grid.**



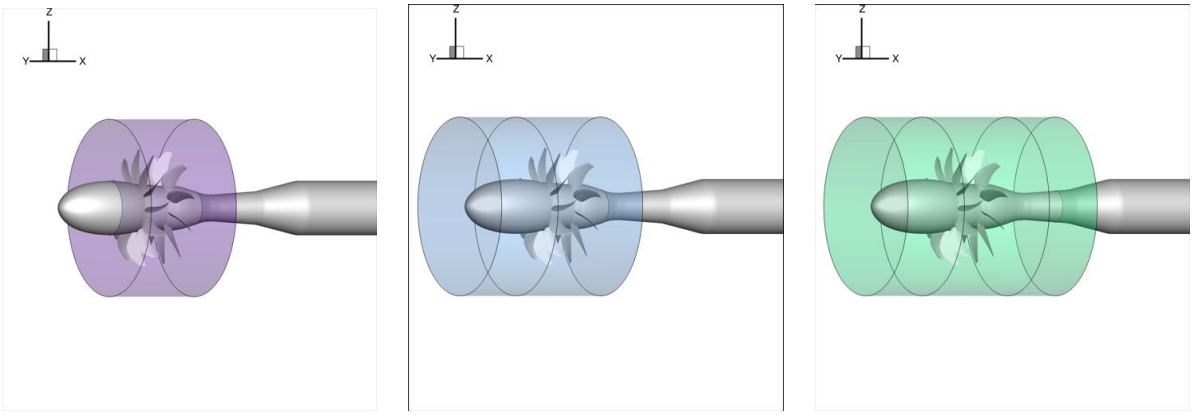

(a) (b)

**Fig. 3 Several views of near and off-body overset grid system (a) zoomed in view of the hub and the finest level of Cartesian off-body block, (b) a zoomed out view of the entire grid system.**

of the grid system in a constant plane are shown in Figure 3. Figure 3 (a) shows a close-up view of the near-body and off-body grids and the sliding-mesh interfaces between rotating and stationary zones. The two rotating zones are colored turquoise for distinction. The finest level of Cartesian off-body grid envelops the model with uniform grid spacing, extending 15 rotor diameters downstream from the aft blade row and two rotor-diameters in the radial direction; see Figure 3 (b).

Hole cutting and connectivity are performed using the modules within the LAVA framework for the overset grid system. The octree-based automatic hole-cutting routines along with an Alternating Digital Tree (ADT) donor search algorithm significantly reduced the necessary wall-time to compute domain connectivity compared to the manual hole-cutting procedure used in previous work[4].

For acoustic propagation, a permeable surface is embedded within the structured overlapping grid system, and tri-linear interpolation is used to record the unsteady flow data onto the face centers of the surface triangulation. For



Surface 1 Surface 2 Surface 3

**Fig. 4 Permeable surfaces used for FW-H propagation.**

the simulations studied here, four permeable acoustic surfaces were generated for the propagation, shown in Figure 4. Each of the surfaces used consists of a tight-fitting cylinder with the same diameter of 0.49 meters. Permeable surface 1 encloses the forward and aft rotors but excludes the wake. Surface 2 surrounds the front end of the hub and the downstream portion of the wake. Surface 3 contains the same front portion of the cylinder as surface 2 but extends much further downstream, stopping at the straight section of the hub.

## V. Computational Results and Discussions

This section presents an analysis of the aerodynamic and aeroacoustic characteristics of the CROR propulsion system for both low- and high-speed configurations using HRLES. To commence, sensitivity studies were conducted to determine the best practices within the LAVA framework for accurately predicting aerodynamic loads and tonal noise of the CROR under nominal takeoff flight conditions. Subsequently, a comprehensive comparison was made between the computed sound pressure level spectrum and the available experimental data for the cruise flight test condition in an 8 by 6 ft supersonic wind tunnel. The high-speed condition analysis aimed to illuminate the impact of the acoustic plate on tonal and broadband noise.

All acoustic data in this publication was presented in terms of shaft order (SO) a dimensionless quantity defined as the ratio of the frequency to the rotational speed of the rotor. This metric helps in easily identifying the individual rotor tones and rotor-rotor interaction tones by relating the frequency of the noise to the rotational characteristics of the rotor system [3, 9].

### A. The Low-Speed Condition – Nominal Takeoff

The low-speed aeroacoustic and aerodynamic predictions, obtained through HRLES simulations within the LAVA computational framework, have undergone comprehensive validation, as reported by Dumlupinar et al. [8]. In this section, our focus is to conduct detailed sensitivity studies to determine a more parameter-independent and reliable CFD/Computational AeroAcoustic (CAA) prediction, building on our previous experience. To accomplish this, first, the acoustic propagation pre- and post-processing parameters were considered; second, a series of HRLES simulations were conducted to assess the appropriate physical time-step needed to capture the essential flow and acoustic features. The grid system employed in this section consists of 321 zones, encompassing approximately 192 million grid points for all sensitivity studies utilizing HRLES-based scale-resolving simulations, with a main physical time step of 1/4 degrees rotation-per-step. For time-step sensitivity studies, two additional time steps were examined, corresponding to 1/2 and 1/8 degrees rotation-per-step. Regardless of time step size, the pseudo-time sub-iteration procedure was executed for 25 iterations or until a 4-orders of magnitude residual reduction was achieved, depending on which criterion was met first.

*1. Sensitivity Studies on Acoustic Propagation*

The parametric studies on acoustic propagation included: the examination of permeable acoustic surfaces, the total number of surface elements, the total number of complete rotor revolutions, and the number of azimuthal positions included in the averaging. To maintain consistency, all comparisons presented here were solely conducted for the simulated Pressure Spectrum Density (PSD) at the microphone aligned with the center of the aft rotor, location 8 in the experimental setup[9]. These comparisons served as a foundation for mutual learning, and the insights gained from these analyses will be applied in future sections.

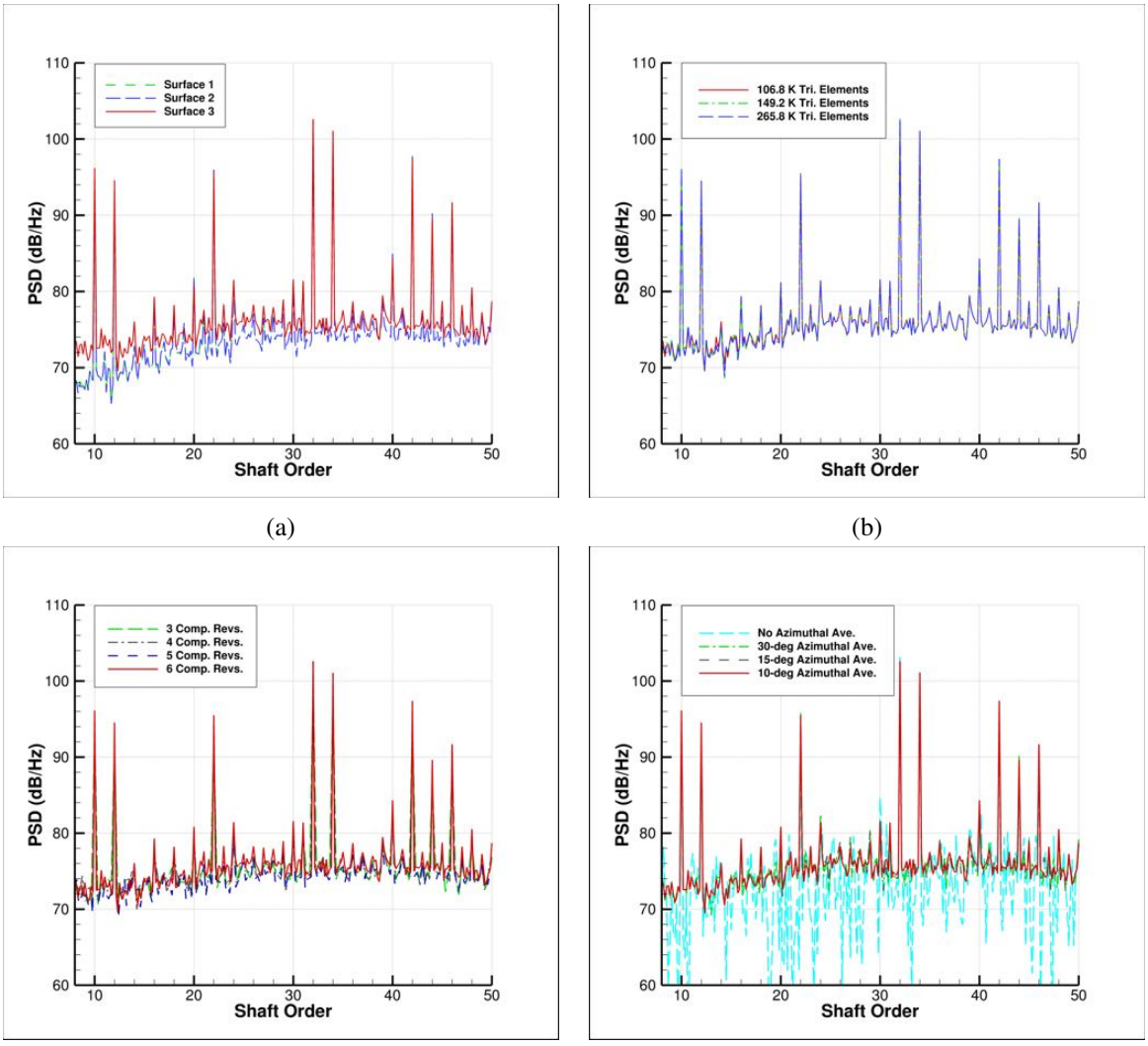



**Fig. 5 The sensitivity study on computed the SPL at Microphone location 8, (a) acoustic permeable surfaces, (b) total number of triangulation elements on permeable surfaces, (c) the total number of complete rotor revolutions, (d) number of circumferential station included in averaging**

The computed pressure spectrum density shown in Figures 5 (a) and 5 (b) were generated by sampling unsteady pressure data over six complete rotor revolutions, resulting in a minimum frequency of 17.5083 Hz. Figure 5 (a) illustrated the effects of acoustic permeable surfaces, as discussed in Section IV. The size of these surfaces directly indicated the amount of recorded unsteady data used to predict acoustic propagations. All three acoustic permeable surfaces matched well to predict tonal noises, ranging from low individual to high combination forward and aft rotor blade frequencies. The predictions for surfaces 1 and 2 overlapped in both tonal and broadband noise, as the upstream

zone of the rotors did not contribute significantly to noise in the low-speed (nominal takeoff) case. In contrast, surface 3 captured more broadband noise structure compared to surfaces 1 and 2. For this reason, and to ensure uniformity in using the same acoustic permeable surface for cruise conditions, permeable surface 3 was chosen for the FW-H acoustic propagation of the dominant tones. Figure 5 (b) illustrated the PSDs for the same microphone location, displaying three refinement levels of acoustic permeable surface 3 with the total triangulated surface elements ranging from 106 to 246 thousand. As expected, the refinement of the acoustic surface was not as crucial as extending the acoustic surface further into the wake region to capture more acoustic features in this frequency range.

The sensitivity analysis of the computed pressure spectrum density to the total number of complete rotor revolutions utilized in the analysis was depicted in Figure 5 (c). The most significant differences in the computed pressure spectrum density, approximately 3 dB, occurred at the larger shaft order levels for both individual and combined blade passing frequencies, observed between three and six complete rotor revolutions. Differences were less than 1.5 dB when comparing four and five complete rotor revolutions to six complete rotor revolutions across the broad spectrum of shaft order levels in tonal noise. The six complete rotor revolutions was chosen to validate against the experimental measurements due to its yielding the lowest first frequency and being the closest to the measured frequency bin level. Figure 5 (d) provides insights into the impact of the number of azimuthal positions included in the averaging process on the computed predicted pressure spectrum density. The methodology for this averaging entailed using the FW-H solver to compute sound pressure at several locations, each at a constant radial distance from the hub centerline. The computed values were then averaged to form the final sound pressure spectral. For comparative analysis, the locations were strategically placed circumferentially at $30^o$, $15^o$, and $10^o$ intervals for azimuthal averaging. Additionally, the PSD without azimuthal averaging was included for comparison. While differences in PSDs between the azimuthal averaging implementations were negligible, the most significant differences in tonal noise were observed at approximately 4 to 5 dB between cases with and without azimuthal averaging, specifically at shaft orders 36 and 40. These shaft orders correspond to the third and fourth blade passing frequencies of the forward and aft blade rows, respectively. Notably, azimuthal averaging played a crucial role in reducing variations in broadband noise levels, bringing them into closer alignment with experimentally reported values, even though they were not shown here.

*2. Temporal Sensitivity Study*

As mentioned earlier, an extensive sensitivity study was conducted using the HRLES approach with physical time steps of 1/2, 1/4, and 1/8 degrees rotation-per-step. In each simulation, the pseudo-time sub-iteration procedure was executed for 25 iterations or until a 4-orders-of-magnitude reduction in residual was achieved, whichever occurred first.

For a qualitative comparison, the computed flow fields with different physical time steps were evaluated alongside available Particle Image Velocimetry (PIV) data obtained from a low-speed test in NASA's 9 by 15 ft acoustic wind tunnel. Figures 6 (a) to (d) present comparisons of the sampling averaging velocity magnitude contours between PIV measurements and the instantaneous contours from scale-resolving simulations on constant axial and circumferential planes once the blade rows completed a full revolution. The HRLES approach effectively captured the location and structure of tip vortices and wake from the forward blades in the cut-planes at all time-step resolutions. Notably, reducing the time step from 1/2 degrees rotation-per-step to a finer resolution demonstrated an improvement in the agreement between the predicted flow field and the measured PIV results, particularly evident in Figures 6 (c) and (d).

**Table 1 Comparison of the computed time-averaged thrust time-steps of $1/2$, $1/4$ and $1/8$ degrees rotation-per-step with experimental measured values.**

| Case | Exp. [9] | 1/2 | 1/4 | 1/8 |
|---|---|---|---|---|
| Thrust [kN] | 2.54 | 2.65 | 2.66 | 2.67 |
| Difference [%] | - | 4.24 | 4.60 | 5.05 |

Table 1 provides a comparison of the aerodynamic loads obtained from the HRLES simulations to the experimental data [9], allowing for a more quantitative assessment of the numerical simulations. The thrust prediction at the nominal takeoff condition was generated by running a minimum of six complete rotor revolutions and time-averaging the results after excluding the first rotor revolution, which contained the initial transients from the impulsive start. The time-averaged computed thrust values showed less than one percent variation among the simulations with different

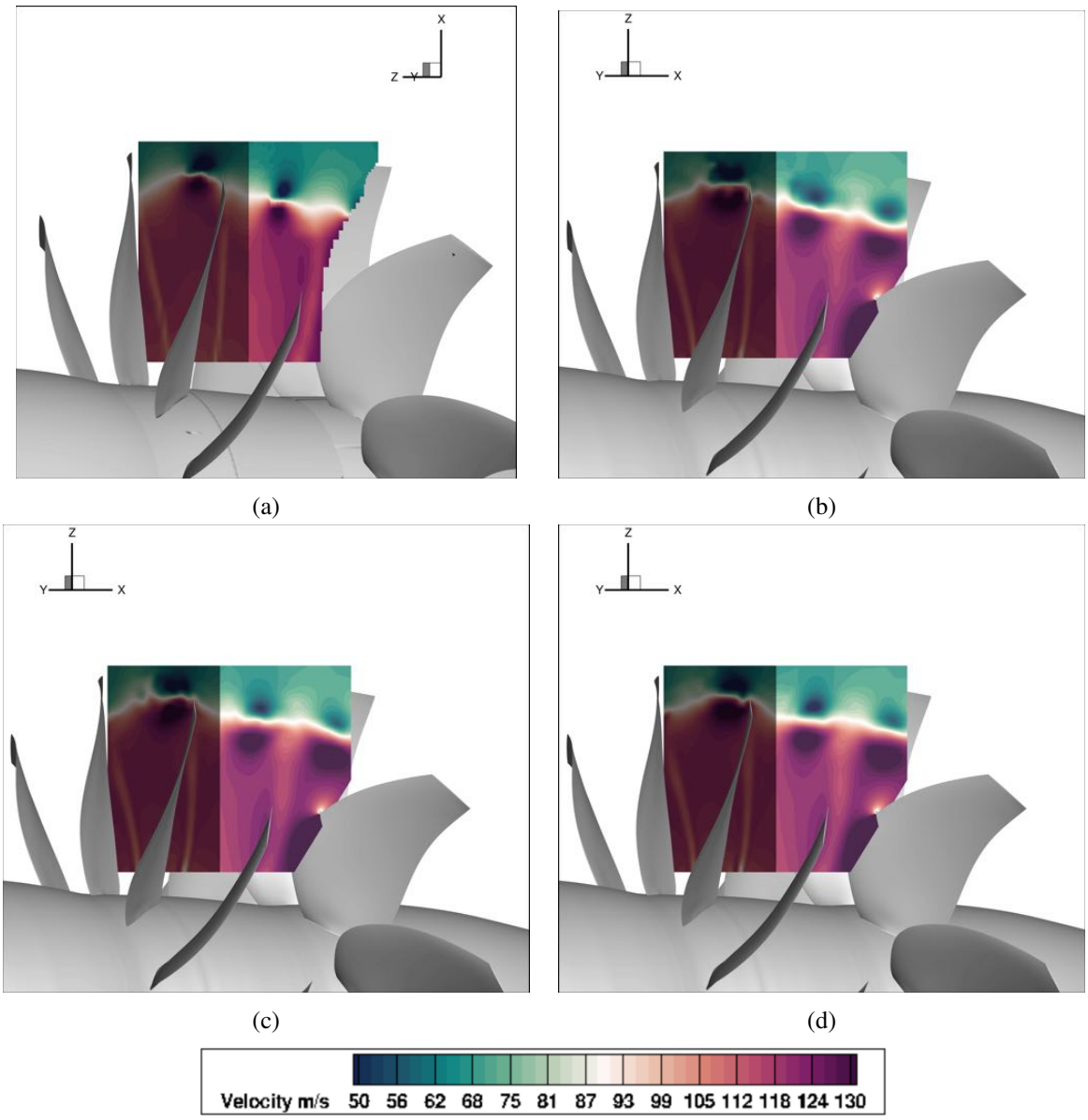


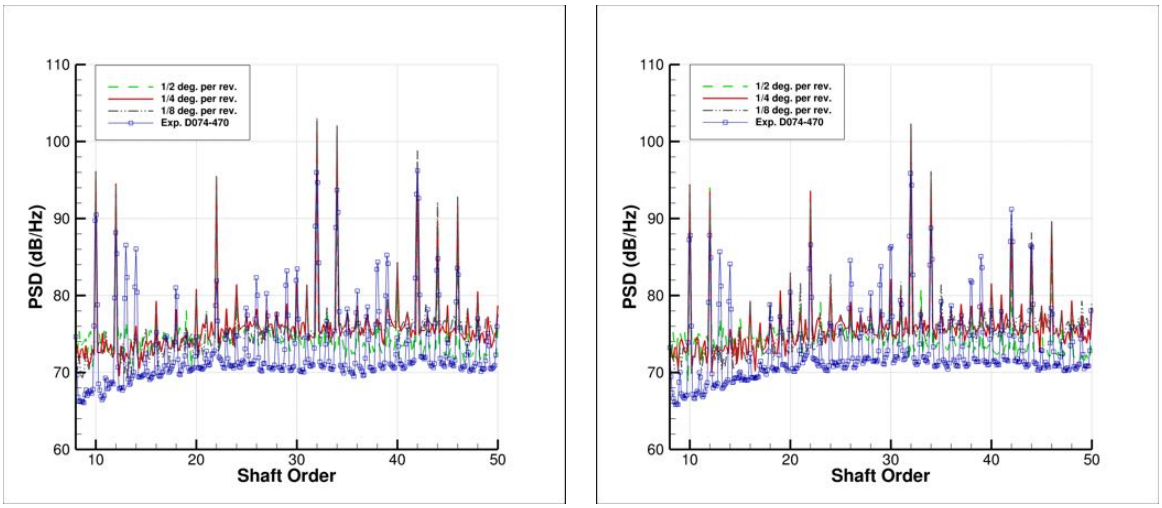

**Fig. 6 Side-by-side comparison of the velocity magnitude contours at constant axial and circumferential cut-planes , (a) PIV measurements, (b) 1/2 degrees rotation-per-step, (c) 1/4 degrees rotation-per-step, (d) 1/8 degrees rotation-per-time-step.**

time steps, ranging from 2.65 to 2.67 kN. These values were 4.24 to 5.05 percent larger than the measured thrust in the experiment. These differences were consistent with previously published results and could be attributed to variations between the "as-built" rig and the CAD model. It was known that small deviations in blade pitch from one blade to the next were likely to exist in the actual test geometry, likely contributing to the observed differences.

Before proceeding to comparisons, the authors wish to draw attention to a minor error in the low-speed case acoustic results as outlined in Dumlupinar et al. [8]. Regrettably, during the conversion from Sound Pressure Level (SPL) to PSD, an inadvertent 3.3 dB decrease occurred in the LAVA predictions, using both URANS and HRLES, constant across the entire spectrum of the shaft order. This error has been rectified in the present publication.

The PSD results presented in this section were generated by sampling unsteady pressure data at every other time step, resulting in states with a sampling rate (1/dt) (Hz) of 37818, 75636, and 151272. These values corresponded

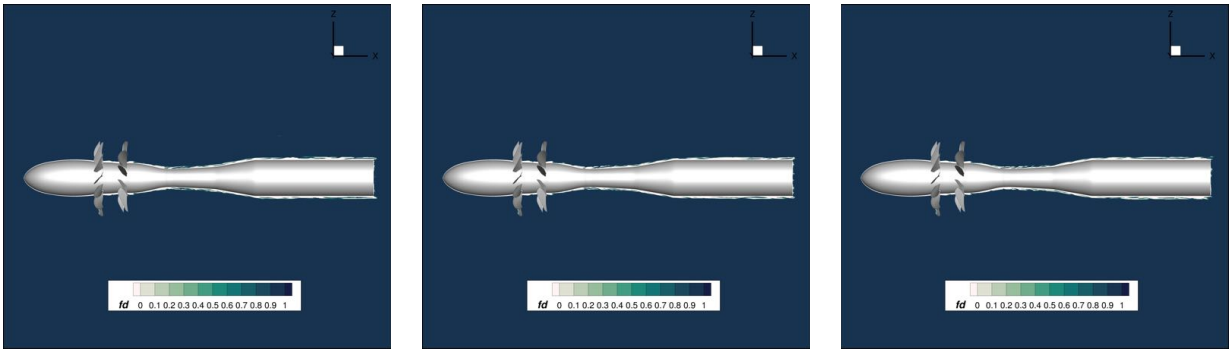
to physical time steps of 1/2, 1/4, and 1/8 degrees rotation-per-step over six complete rotor revolutions, yielding a common state frequency of 17.5083 Hz, representing the lowest frequency (1/T) (Hz). The data was interpolated onto the permeable acoustic surface 3, described in Section IV, embedded within the structured overset grid system. For comparison, the sound pressure was generated circumferentially 10 degrees apart for azimuthal averaging to form the final pressure spectral density. The comparison of the calculated noises using the HRLES simulations versus experimental measurement (D074 - 470 [9]) is shown in Figures 7 as a function of shaft order (SO) up to 50. The predicted tones from the HRLES simulation associated with the forward and aft rotor row blade passing frequencies matched well with the experimentally measured tones, and no observable spurious tones were present in the signal. The individual dominant tones related to rotor rows were identified with an integer multiplier of forward and aft row blade counts, 12 and 10 respectively. Rotor-to-rotor interaction tones were recognized through the summation of these individual tones. In the analysis, the simulated individual tones exhibited an over-prediction of approximately 6 dB compared to the measured values. This over-prediction became more pronounced as the physical time step was refined for both low and high blade passing frequencies. These observations held consistently at both microphone locations, as illustrated in Figure 7. However, an exception was noted for the third blade passing frequency of the aft blade row — SO 30 — at microphone locations 8 and 9, where simulations with all physical time-steps consistently under-predicted the measured tones. Once again, HRLES simulations tended to over-predict rotor-to-rotor interaction tones, specifically those corresponding to SO values of 22, 32, 34, 42, 44, and 46, spanning low to high frequencies. The differences between simulated and measured tones were mostly below 6 dB, with the exception of SO 22 and 46. These exhibited an approximately 11 dB difference for microphone locations 8 and 9, respectively.




(a) (b)

**Fig. 7 The computed PSD at (a) Microphone locations 8, and (b) Microphone locations 9 for the low-speed condition.**

All three physical time steps tested in this work behaved very similarly, with tonal noise predictions showing slight differences in magnitude. These differences generally increased as the time steps were refined but did not exceed 2 dB. This might be attributed to the additional protection in the LAVA HRLES implementation, which directly correlates with the physical time steps of the simulation. Figures 8 (a) to (c) display contour plots illustrating the instantaneous shielding function, $f_D$, at the hub's centerline. These plots demonstrate the behavior of the shielding function, preserving the boundary layer by maintaining the URANS mode. Notably, a RANS closure was implemented within the boundary layer around the hub, where $f_D$ approached 0.0. Beyond the boundary layer, the LES mode was activated (i.e., $f_D$ = 1.0), and there was no observed spurious switching back to the URANS mode. Despite significant variations in time steps between these cases, Figures 8 (a) to (c) indicate that the shielding function behaved as intended.

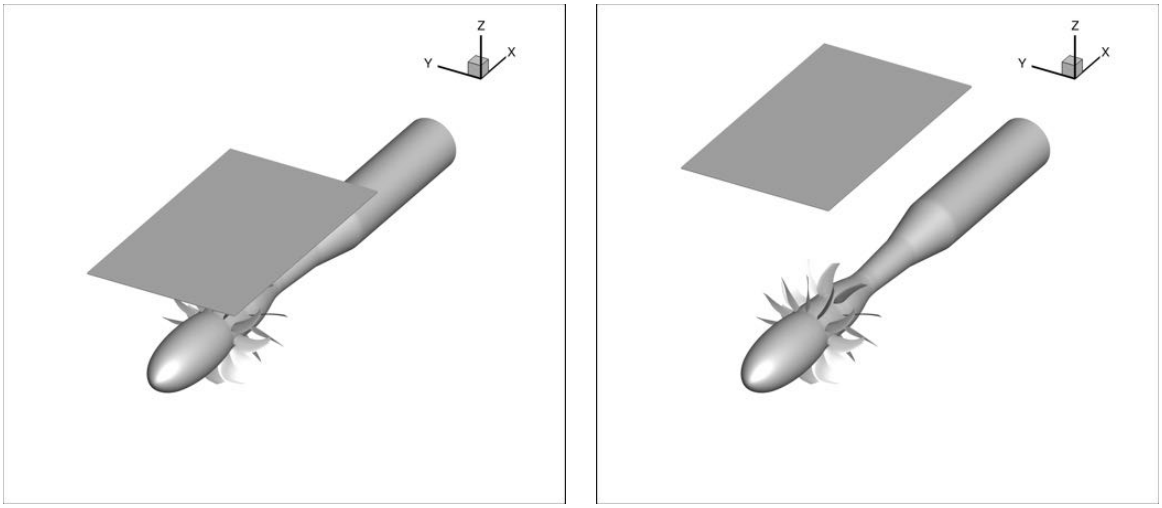


(a) (b) (c)

**Fig. 8 Contour plots of the instantaneous shielding function for the following physical time step of (a) 1/2 degrees rotation-per-step, (b) 1/4 degrees rotation-per-step, and (c) 1/8 degrees rotation-per-step.**

### B. The High-Speed Condition – Cruise Condition

A comprehensive comparison was conducted between the computed SPL spectrum and the available experimental data [9] for the cruise flight test condition in an 8 by 6 ft supersonic wind tunnel, as thoroughly documented by Dumlupinar et al. [8]. The analysis revealed an excellent correlation between measured and computed tonal noise using the HRLES approach while also exposing a significant under-prediction of broadband noise. A key factor contributing to this limitation in the simulation was the experimental measurements being conducted in a supersonic wind tunnel, known for its inherently noisy environment, despite the test section's sides and roof being constructed with porous walls. Additionally, the simulation did not include the "acoustic plate" and "test rig" support structures, which undoubtedly contributed to the observed broadband noise in the measurements. This aspect of the experimental condition was confirmed through tare testing conducted during the measurement campaign. As reported by Stephens [9], the tare spectra, while significantly lower than the tones measured with contra-rotating blade rows, curiously exhibited higher broadband spectra for frequencies less than 3200 Hz at the inflow Mach number of 0.78. It is noteworthy that this inflow condition was the same, but the forward and aft blade set pitch angles were slightly different from the cruise condition studied by Dumlupinar et al. [8] and in the present work.




(a) (b)

**Fig. 9 The computational domains include the acoustic plate vertical positions at (a) 0.51 meters, and (b) 1.16 meters away from the rotating axis.**

This section illuminates the influence of the acoustic plate on both tonal and broadband noise. The acoustic plate was utilized as the holder for the Kulite pressure sensors during the experimental study in the high-speed configuration. In pursuit of this understanding, adjustments were made to the overset grid system by incorporating the acoustic plate component at two vertical positions — 0.51 and 1.16 meters away from the rotating axis, as illustrated in Figure 9. The dimensions and positions of the acoustic plate with respect to the test article were extracted from publicly available documentation [3, 9, 17]. It is important to note that including the acoustic plate introduced the possibility of acoustic waves reflecting off its surface. For this reason, the off-body Cartesian mesh system was also modified to have a fine enough mesh to envelop both forward and aft rotor rows, as well as the acoustic plate, without making any changes to the near-body grid system described in Section IV. This straightforward modification to the grid system enabled the numerical resolution of wave propagation from near-field sources to far-field observers, thereby eliminating the need for a CAA solver. The same specifically developed off-body Cartesian mesh was utilized for both acoustic plate positions, as well as the case without the acoustic plate, to determine the effects of grid system changes. In the simulations for the cruise condition, the revised overset grid system comprised 384 zones, containing approximately 294 million grid points in cases involving the acoustic plate. Conversely, for the case without the acoustic plate, it consisted of 374 zones with approximately 274 million grid points. A constant physical time step of 1/4 degrees rotation-per-step was employed for all simulations. The pseudo-time sub-iteration procedure involved 25 iterations or continued until a 4-orders-of-magnitude reduction in residuals was achieved, whichever criterion was satisfied first. This temporal resolution proved to be adequate for capturing meaningful flow and acoustic features for this configuration, as demonstrated by the work of Housman and Kiris [4]. The effectiveness of this approach was further validated by Dumlupinar et al. [8] using the sliding mesh option. Closely following the procedures outlined by Stephens [9] and Envia [3], the computed sound pressure levels (SPL) using HRLES approach were compared with the experimental results reported by Stephens [9].

### *1. The dInfluence of the Acoustic Plate on the Computed Flow Field*

This subsection offers a qualitative characterization of the influence of the acoustic plate on the flow field, comparing the effects of its position relative to the rotational axis of the model size of the contra-rotating open rotor. Figure 10 plotted the instantaneous (a) to (c) normalized pressure difference contour plots and (d) to (f) the magnitude of the density gradient contours on the slice through the centerline of the hub. The pressure fields revealed the formation of shocks traveling upstream from the rotor blades due to the displacement of air by the supersonically moving blade tips at the specified RPM. Notably, a weak shock just downstream of the aft blade row and a more pronounced fish-tail shock as the hub radius transitioned from a narrow to a wider cross-section were observed in Figures 10 (a) to 10 (c) under this flow condition. In the presence of the acoustic plate, it is essential to highlight that waves generated by the movements of both forward and aft blades reflected off the plate, regardless of its position, as illustrated in Figures 10 (b) and 10 (c). The density gradient magnitude, as shown in Figures 10 (d) to (f), not only illustrates acoustic and reflecting waves but also vividly portrays the downstream convection of tip vortices. The interaction of these tip vortices with the strong shock at the hub transition formed an additional acoustic noise source. In addition, the density gradient magnitude contour revealed intricate flow features near the hub, encompassing both sides of the acoustic plate and its wake, providing clear visibility.

In Figures 11 (a) to (i), contour plots illustrated the instantaneous normalized pressure from HRLES simulations. These plots showcase constant stream-wise slices through the forward rotor, between the two rotor rows, and the aft rotor for three computational domain configurations. Figures 11 (a) to (c) showed the wave pattern dominated by the clockwise rotation of the forward rotor near the blades, with a weak interaction with the aft rotor observed vertically away from the blade tips. As anticipated, strong interaction between the waves generated by both the forward and aft rotors was evident, as shown in Figures 11 (d) to (f). The aft rotor exhibited wave patterns associated with the counter-clockwise rotation of the aft blades near the hub, as seen in the bottom row contour plots of Figure 11 across different computational domain configurations. In the presence of the acoustic plate, waves directly radiated from the forward and aft rotor rows interacted with the acoustic plate and the pressure sensors (Kulites) it held. These interactions were more pronounced when the acoustic plate's vertical position was closer to the source, as observed in Figures 11 (b), (e), and (h). Importantly, accurately predicting the acoustic field in closed approximations was crucial for understanding the interaction between the propulsor-wing, as well as the propulsor-fuselage or -cabin. The confidence gained in the analysis tools proved instrumental in developing new single-aisle aircraft targeting the 2030s. Additionally, this advancement supported NASA Aeronautics and other Sustainable Flight National Partnership (SFNP) participants in getting closer to a common goal of achieving net-zero carbon emissions by 2050.

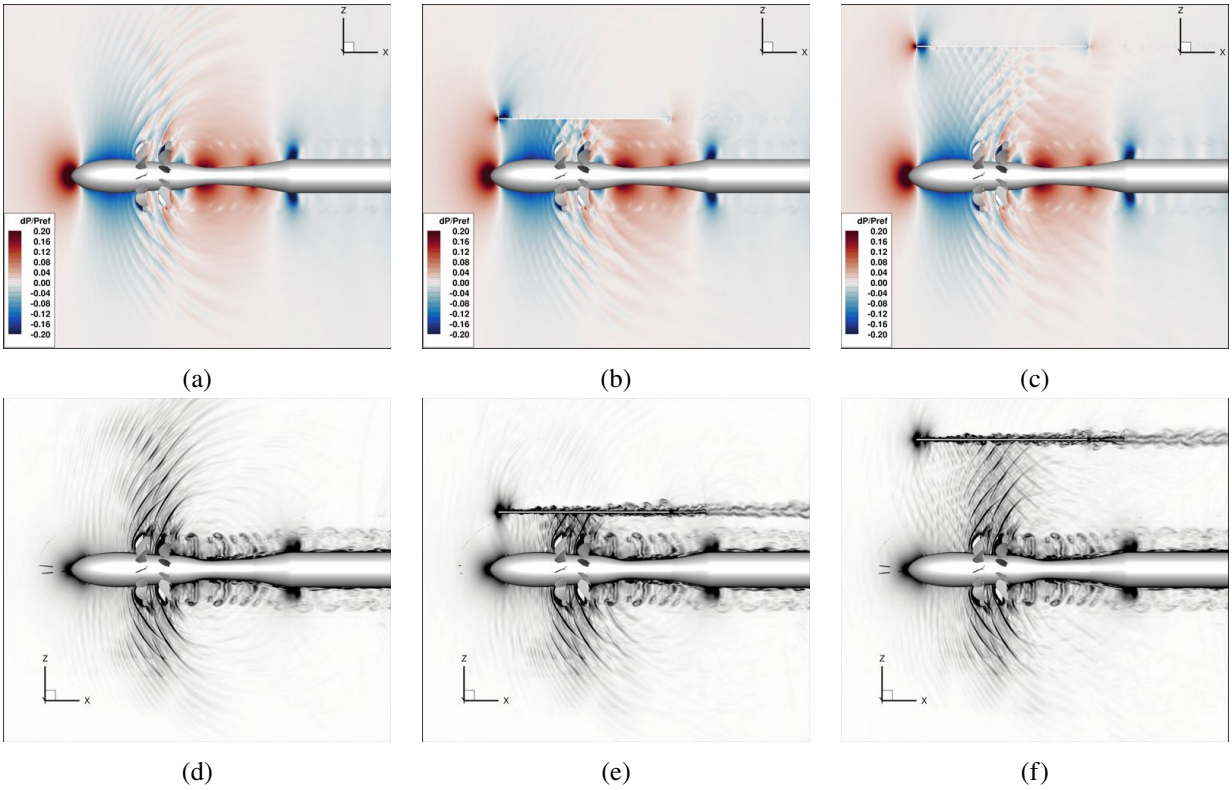



**Fig. 10 Comparison of the instantaneous computational flow field with and without the influence of the acoustic plate at the same total physical time, (a) normalized pressure difference without acoustic plate, (b) normalized pressure differences acoustic plate position at 0.51 meters, (c) normalized pressure differences acoustic plate position at 1.16 meters, (d) magnitude of the density gradient without acoustic plate, (e) magnitude of the density gradient acoustic plate position at 0.51 meters, (f) magnitude of the density gradient acoustic plate position at 1.16 meters**

*2. Aeroacoustic Tones Comparison*

The SPL spectra computed in this section were derived by sampling unsteady pressure data at every other time step, leading to a sampling rate (1/dt)(Hz) of 82176. These values corresponded to physical time steps of 1/4 degrees per revolution over six complete rotor revolutions, resulting in a common state frequency of 19.022 Hz, representing the lowest frequency (1/T).

Figures 12 (a) and (b) depicted the comparison between the computed SPL obtained from HRLES simulations, with and without the inclusion of the acoustic plate in the computational domain. These results were contrasted with measurement runs 2969 and 2962 from the experimental campaign [9]. It is important to emphasize that the experimentally measured data presented in Figures 12 (a) and (b) remains unaltered, without any additional modifications. In contrast to Envia's suggestion [3] of subtracting a constant 6 dB from the entire measured spectrum when the computational domain excludes the acoustic plate. Moreover, the computed SPL results were acquired by directly sampling unsteady pressure data from the computational domain at the precise Kulite locations corresponding to the measurements, without employing azimuthal averaging. The HRLES predictions effectively captured tones associated with the forward and aft rotor rows at individual blade passing frequencies (BPFs), aligning well with experimental results at two vertical positions. However, a noteworthy exception was observed—a significant under-prediction occurred in the fourth harmonic of the forward blade passing frequency, particularly at the SO of 48. This discrepancy was consistent for simulations with and without the acoustic plate at the vertical position of 0.51 meters. The HRLES simulations correctly predicted rotor-to-rotor interacting tones, which are linked to linear combinations of the two blade passing frequencies. This alignment was observed in simulations that included the acoustic plate, except for the SO of 42, 44, and 46 when the acoustic plate was positioned at 0.51 meters vertically. The comparisons of computed sound

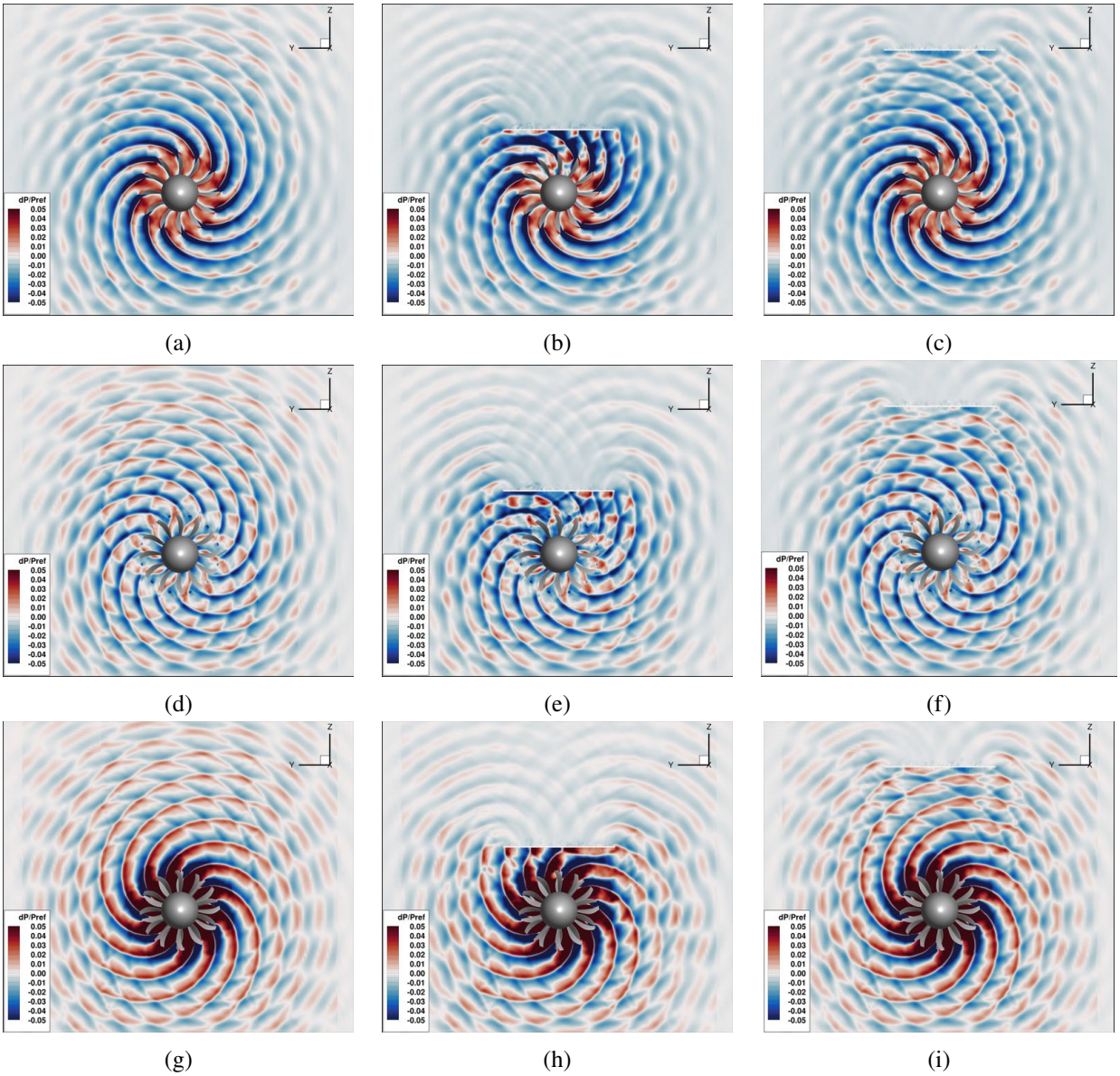
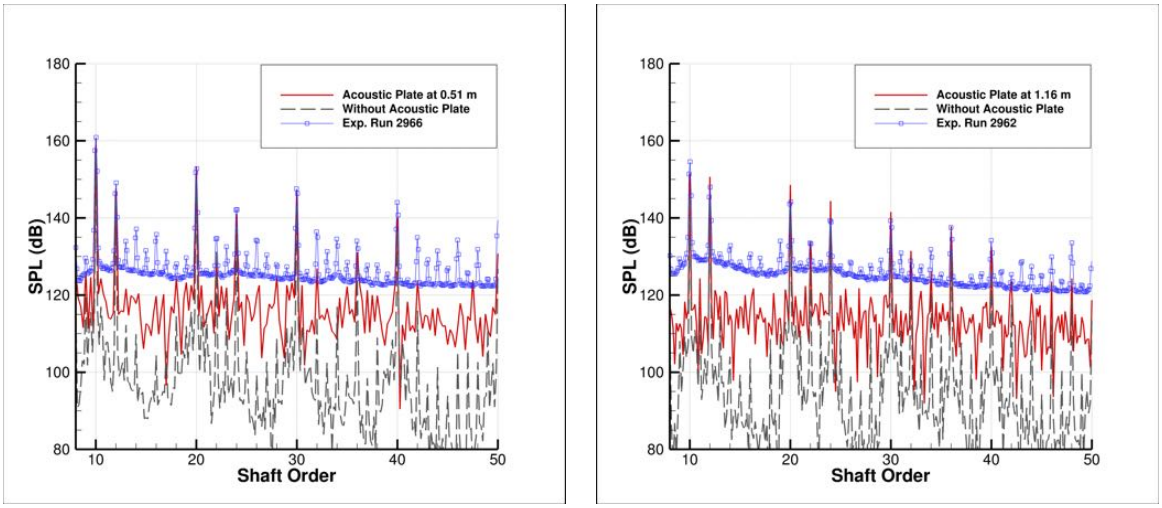



**Fig. 11 Comparison of contour plots of normalized pressure difference on constant stream-wise slices of the instantaneous computational flow field with and without presence of the acoustic plate at the same total physical time: through the forward rotor row (a) without acoustic plate, (b) acoustic plate position at 0.51 meters, (c) acoustic plate position at 1.16 meters; between the two rotor rows (d) without acoustic plate, (e) acoustic plate position at 0.51 meters, (f) acoustic plate position at 1.16 meters; through the aft rotor row (g) without acoustic plate, (h) acoustic plate position at 0.51 meters, (i) acoustic plate position at 1.16 meters**

pressure levels revealed that the acoustic plate induced broadband noise, aligning with expectations based on the flow visualizations presented in 10 (a) to (f).

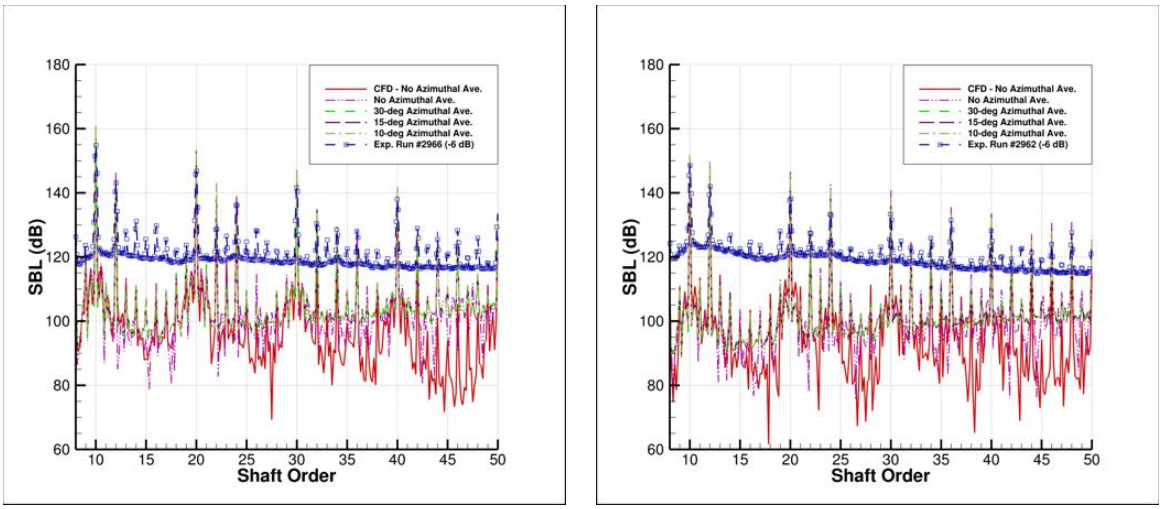
Figure 13 offers insights into how varying the number of azimuthal positions in the averaging process influences the computed SPL using the coupled CFD/CAA approach. The measured data has been adjusted by subtracting 6 dB to compensate for the doubling of acoustic waves at the acoustic plate. The methodology employed for this averaging mirrors that described in the Section V.A. A significant observation emerged from the comparisons in Figure 13: irrespective of whether pure CFD or coupled CFD/CAA results were employed, azimuthal averaging consistently

enhanced the quality of predictions. This improvement was particularly pronounced at the high-order individual and combined blade passing frequencies, observed at both vertical positions examined in this section.




(a) (b)

**Fig. 12 The comparison of sound pressure level (SPL) spectrum using only CFD solutions at Kulite 9 located above the aft rotor at a vertical distance of (a) 0.51 meters and (b) 1.16 meters from the rotational axis of the system**




(a) (b)

**Fig. 13 Sound pressure level (SPL) spectrum using CFD/CAA approach at Kulite 9 located above the aft rotor at a vertical distance of (a) 0.51 meters and (b) 1.16 meters from the rotational axis of the system**

## VI. Summary

The LAVA solver framework, employing structured curvilinear overlapping grids and a sliding mesh approach, was successfully utilized to predict the aerodynamic behavior of a model-scale CROR propulsion system. The framework was applied to both low-speed (nominal takeoff) and high-speed (cruise) configurations of the CROR. Extensive sensitivity

studies on the time-step were conducted to establish optimal practices for HRLES analysis of the CROR's unsteady flow field. The computed flow field, integrated aerodynamic forces, and acoustic predictions obtained from the LAVA solver exhibited excellent agreement under both nominal takeoff and cruise test conditions. The PIV measurements, obtained through sampling averaging, aligned well with the instantaneous velocity magnitude contours generated using HRLES with three different time steps. Overall, the results summarized in this publication instill significant confidence in the LAVA best practices for predicting tonal and broadband noise, as well as for assessing interactions among the propulsor, wing, fuselage, and/or cabin.

## VII. Acknowledgements

This work was partially funded by the Advanced Air Transport Technology (AATT) project and the Transformational Tools & Technologies (TTT) project under NASA Aeronautics Research Mission Directorate (ARMD). Computer time has been provided by the NASA Advanced Supercomputing (NAS) facility at NASA Ames Research Center.

## References

[1] Kiris, C., Barad, M., Housman, J., Sozer, E., Brehm, C., and Moini-Yekta, S., "The LAVA Computational Fluid Dynamics Solver," *52st AIAA Aerospace Sciences Meeting, National Harbor, Maryland*, 2014. AIAA-2014-0070.

[2] Kiris, C. C., Housman, J. A., Barad, M. F., Brehm, C., Sozer, E., and Moini-Yekta, S., "Computational framework for Launch, Ascent, and Vehicle Aerodynamics (LAVA)," *Aerospace Science and Technology*, Vol. 100, No. 55, 2016, pp. 189–219.

[3] Envia, E., "Contra-Rotating Open Rotor Tone Noise Prediction," *20th AIAA/CEAS Aeroacoustics Conference, Atlanta, Georgia*, 2014. AIAA-2014-2606.

[4] Housman, J. A., and Kiris, C. C., "Structured Overlapping Grid Simulations of Contra-Rotating Open Rotor Noise," *54th AIAA Aerospace Sciences Meeting*, 2016. AIAA-2016-0814.

[5] Brehm, C., Barad, M., and Kiris, C., "An Immersed Boundary Method for Solving the Compressible Navier-Stokes Equations with Fluid-Structure Interaction," *54th AIAA Aerospace Sciences Meeting, San Diego, CA*, 2016. AIAA-2016-0815.

[6] Brehm, C., Barad, M., and Kiris, C., "Open Rotor Aeroacoustic Analysis with an Immersed Boundary Method," *54th AIAA Aerospace Sciences Meeting, San Diego, CA*, 2016.

[7] Nark, D., Jones, W., Boyd, D., and Zawodny, N., "Isolated Open Rotor Noise Prediction Assessment Using the F31A31 Historical Blade Set," *54th AIAA Aerospace Sciences Meeting, San Diego, CA*, 2016.

[8] Dumlupinar, E., Housman, J. A., Kenway, G. K., and Kiris, C. C., "Unsteady RANS and Scale Resolving Simulations of Open Rotor Noise," *AIAA SciTech Forum, National Harbor, MD*, 2023. AIAA 2023-0028.

[9] Stephens, D. B., "Data Summary Report for The Open Rotor Propulsion Rig Equipped With F31/A31 Rotor Blades," *NASA/TM-2014-216676*, 2014.

[10] Koch, J. R., Dumlupinar, E., Housman, J. A., Kiris, C. C., Patel, M. M., Kleb, B., Brauckmann, G. J., and Alter, S. J., "CFD analysis of Space Launch System solid rocket booster separation within the Langley Unitary Plan Wind Tunnel," *AIAA Aviation 2021 Forum,* AIAA Paper 2021-2966, 2021.

[11] Deck, S., and Renard, N., "Towards an Enhanced Protection of Attached Boundary Layers in Hybrid RANS/LES Methods," *Journal of Computational Physics*, Vol. 400, 2020, p. 108970.

[12] Kiris, C., and et al., "High-Lift Common Research Model: RANS, HRLES and WMLES Perspectives for $C_{L_{\max}}$ Prediction Using LAVA," *AIAA SCITECH 2022 FORUM*, 2022.

[13] Housman, J. A., Stich, G.-D., Kocheemoolayil, J. G., and Kiris, C. C., "Predictions of Slat Noise from the 30P30N at High Angles of Attack using Zonal Hybrid RANS-LES," *25th AIAA/CEAS Aeroacoustics Conference*, 2019, p. 2438.

[14] Ffowcs Williams, J. E., and Hawkings, D. L., "Sound generation by turbulence and surfaces in arbitrary motion," *Philosophical Transactions of the Royal Society of London A*, Vol. 342, 1969, pp. 264–321.

[15] Chan, W., Gomez, R., Rogers, S., and Buning, P., "Best Practices in Overset Grid Generation," *32nd AIAA Fluid Dynamics Conference and Exhibit, St. Louis, Missouri*, 2002. AIAA-2002-3191.

[16] Chan, W., "Developments in Strategies and Software Tools for Overset Structured Grid Generation and Connectivity," *20th AIAA Computational Fluid Dynamics Conference*, 2012.

[17] Hoff, G., "Experimental Performance and Acoustic Investigation of Modern, Counterrotating Blade Concepts," *NASA Contractor Report 185158*, 1990.